# Imaging the Traction Stresses Exerted by Locomoting Cells with the Elastic Substratum Method

M. Dembo,* T. Oliver,‡ A. Ishihara,‡ and K. Jacobson‡

*Department of Biomedical Engineering, Boston University, Boston, Massachusetts 02215, and ‡Department of Cell Biology and Anatomy, University of North Carolina at Chapel Hill, Chapel Hill, North Carolina 27599 USA

ABSTRACT The cytoskeletal activity of motile or adherent cells is frequently seen to induce detectable displacements of sufficiently compliant substrata. The physics of this phenomenon is discussed in terms of the classical theory of small-strain, plane-stress elasticity. The main result of such analysis is a transform expressing the displacement field of the elastic substrate as an integral over the traction field. The existence of this transform is used to derive a Bayesian method for converting noisy measurements of substratum displacement into "images" of the actual traction forces exerted by adherent or locomoting cells. Finally, the Monte Carlo validation of the statistical method is discussed, some new rheological studies of films are presented, and a practical application is given.

## GLOSSARY OF SYMBOLS*

$A_T$ ≡ Total area of $\Omega$ (10)
$A^k$ ≡ Area integral of $S^k$ (11)
$\alpha$ ≡ Index of the coordinate directions in the Cartesian plane
$\beta$ ≡ Index of the coordinate directions in the Cartesian plane
$\mathcal{C}^2$ ≡ A statistical measure of "complexity" (16)
$\mathbf{d}$ ≡ $(d_1, d_2)$ ≡ A generic displacement vector (2)
$\hat{\mathbf{d}}^p$ ≡ $(\hat{d}_1^p, \hat{d}_2^p)$ ≡ Experimental displacement of the $p$th particle (7)
$\mathbf{d}^p$ ≡ $(d_1^p, d_2^p)$ ≡ Theoretical displacement of the $p$th particle (7).
$\delta_{\beta\beta}$ ≡ A generic component of Kronecker's delta (2)
$\delta T_\alpha^k$ ≡ Standard deviation of the nodal tractions; $T_\alpha^k$
$E$ ≡ Young's modulus of the substratum material (2)
$E_s$ ≡ Surface Young modulus of the substratum (3)
$\epsilon_{\alpha\beta}$ ≡ A generic component of the two-dimensional Cartesian strain tensor (2)
$\mathbf{f}$ ≡ $(f_1, f_2)$ ≡ A generic position vector
$\mathbf{f}^k$ ≡ $(f_1^k, f_2^k)$ ≡ Position of the $k$th node of a mesh (8)
$g_{\alpha\beta}$ ≡ A component of the two-dimensional displacement Green's function (5)
$h$ ≡ The thickness of the elastic membrane (1)
$H$ ≡ A particular element of $\{H\}$ (13)
$\{H\}$ ≡ The universe of all the theories to be tested (13)
$j$ ≡ An integer between 0 and N (8)
$k$ ≡ An integer between 0 and N (8)
$\lambda$ ≡ Smallest detectable traction density (18)
N ≡ The number of nodes in a mesh (8)
$\nu$ ≡ Possion's ratio of the substratum material (2)
$O_1$ ≡ An observer who defines complexity according to Eq. 17
$O_2$ ≡ An observer who defines complexity according to eq. 19
$\Omega$ ≡ The interior of domain within which tractions occur (8)
P ≡ Total number of particle observations in an experiment (7)
$p$ ≡ An integer between 1 and P
$P(H)$ ≡ The a priori probability of $H$ (13)
$P(H \mid X)$ ≡ Probability of $H$ after experiment $X$ (13)
$P(X \mid H)$ ≡ Probability of $X$ given that $H$ is true (13)
$\mathbf{r}^p$ ≡ $(r_1^p, r_2^p)$ ≡ Error of the observed displacement of the $p$th particle (7)
$s$ ≡ Pixel resolution of a discretized image (7)
$S^k$ ≡ Shape function of the $k$th node of a mesh (8)
$S_{\bar{X}}$ ≡ A normalization constant (13)
$\sigma$ ≡ Resting drumhead tension of the substratum (2)
$\sigma_{\alpha\beta}$ ≡ A component of the two-dimensional Cartesian stress tensor (1)
$\mathbf{T}$ ≡ $(T_1, T_2)$ ≡ A traction density vector field (1)
$\mathbf{t}^k$ ≡ $(T_1^k, T_2^k)$ ≡ A traction density vector at the $k$th mesh node (12)
$\mathbf{w}^0$ ≡ $(w_1^0, w_2^0)$ ≡ Drift error (7)
$\mathbf{w}^k$ ≡ $(w_1^k, w_2^k)$ ≡ Imaging degree-of freedom at the $k$th mesh node (9)
$\bar{\mathbf{w}}$ ≡ $(\bar{w}_1, \bar{w}_2)$ ≡ Area average of the $\mathbf{w}^k S^k$ (12)
$\mathbf{x}$ ≡ $(x_1, x_2)$ ≡ A generic position vector
$\mathbf{x}^p$ ≡ $(x_1^p, x_2^p)$ ≡ Reference position of the $p$the particle (7)
$\{X\}$ ≡ Set of all possible outcomes of an experiment (13)
$X$ ≡ An element of $\{X\}$ realized in a particular experiment (13)
$\chi^2$ ≡ A statistical measure of goodness to fit (15)

## INTRODUCTION

In studies of cell locomotion and motility, a major goal has been to correlate the kinematic observations available by direct cytological methods and the underlying processes of cytoskeletal force generation (see Sheetz, 1994; Lee et al., 1993, 1994; Evans, 1993; Condeelis, 1993; Lauffenburger, 1991; Cramer et al., 1993). An important contribution to this program (Harris et al., 1980) was the basic idea of observing the reactions of elastic substrata to the presence of locomoting or adhering cells. To implement this idea Harris and his co-workers developed a procedure for fabricating highly compliant yet stable films made of silicone rubber. They subsequently demonstrated that cells could induce large lateral displacements and wrinkling when placed upon such substrata. Recently some refinements to the basic method of Harris were introduced to facilitate

*Received for publication 10 July 1995 and in final form 7 December 1995.*

Address reprint requests to Dr. Michael Dembo, Department of Biomedical Engineering, Boston University, 44 Cummington Street, Boston, MA 02215-2407. Tel.: 617-353-1671; Fax: 617-353-6766; E-mail: mxd@organelle.ba.edu.



0006-3495/96/04/2008/15 $2.00

*Where possible, an equation number apropos of each defined symbol is given in parentheses following definition.

more reproducible and quantitative measurements of the elastic deformation (Oliver et al., 1995; Lee et al., 1994).

Measurements of substratum deformation, even if they are very accurate, are merely secondary reflections of the underlying biologically generated tractions. Therefore, to deduce the actual traction stresses being exerted upon a substratum point by point it is necessary to process the information inherent in displacement measurements by some sort of statistical procedure. Our approach to the calculation of such "traction images" starts by approximating the distribution of traction stresses acting on the substratum as a superposition of elementary "delta function" influences. Next, given a set of noisy displacement observations, we use standard methods of data fitting to find the most likely amplitudes and locations of the elementary influences. Below, we explain these matters in more detail. See the Appendix for definitions of notation used.

## COMPUTING DISPLACEMENTS GIVEN TRACTIONS

Consider a infinite flat membrane or plate composed of a uniform isotropic elastic material and introduce Cartesian coordinates $[x_1, x_2, x_3]$ such that the center of the membrane is coincident with the plane, $x_3 = 0$. Presuming that the only external loads acting on the membrane consist of tangential tractions on its upper surface, one may consistently reduce the dimensionality of the problem by invoking a standard "plane stress" approximation. If $\sigma_{\alpha\beta}$ are the components of the stress tensor, $T_\alpha$ the components of the applied traction stress, and $h$ the membrane thickness, then we may write the thickness-averaged condition for stress equilibrium as

$$h(\partial_1\sigma_{\alpha 1} + \partial_2\sigma_{\alpha 2}) + T_\alpha = 0. \tag{1}$$

Details of the arguments leading to this plane stress approximation are given by many authors; a standard source is Landau and Lifshitz (1986).

In addition to a stress balance, one must consider that the membrane has some degree of elastic compliance and that it will therefore deform slightly from its reference state as a result of any applied loads. In particular, a point in the midplane of the membrane with initial position $\mathbf{x} = (x_1, x_2)$ will be displaced to a new equilibrium position $\mathbf{x}' = \mathbf{x} + \mathbf{d}$. Letting $\epsilon_{\alpha\beta} \equiv 0.5(\partial_\alpha d_\beta + \partial_\beta d_\alpha)$ be the Cartesian strain tensor associated with this deformation field, one can easily obtain the appropriate thickness averaged stress-strain relation by combining the three-dimensional form of Hooke's law with the plane stress requirement:

$$\sigma_{\alpha\beta} = \frac{E}{(1+\nu)}\epsilon_{\alpha\beta} + \frac{E\nu(\epsilon_{11}+\epsilon_{22})}{(1-\nu^2)}\delta_{\alpha\beta} + \bar{\sigma}\delta_{\alpha\beta}. \tag{2}$$

There are three constant moduli in this constitutive law: $\nu$, the Poisson ratio; $E$, the Young modulus; and $\bar{\sigma}$, which is the prestressed drumhead tension. For the silicone rubber films used in the current study, the three-dimensional material that composes the film is incompressible, and Poisson's ratio is therefore certainly very close to 0.5.

We cannot overemphasize the importance of an adequate level of drumhead prestress, $\bar{\sigma}$. Basically this is because a sheet under some tension from the boundaries tends to remain flat and resists wrinkling under the action of tangential tractions. One the other hand, if the $\bar{\sigma}$ of a film is small or negative, then the only factor to prevent wrinkling when tractions are applied is its bending rigidity. It is easy to estimate that the latter is not adequate to prevent wrinkling in studies of cell tractions because the films are very thin and because the silicone rubber is highly compliant. Thus, in the early studies by Harris and coworkers, wrinkles dominated the results obtained. Although wrinkles do provide some evidence of the existence of cellular tractions, they are disastrous as far as any hope of quantitative deformation analysis is concerned. The previously described methodology for manufacture of silicone rubber membranes fortuitously produced films with a large prestress. This serendipitous development was thus an essential precondition for the current analysis (Oliver et al., 1995; Lee et al., 1994).

Substituting Eq. 2 into the equations for stress equilibrium, we finally obtain coupled second-order partial differential equations for the components of equilibrium deformation in the midplane:

$$\begin{aligned}
&\frac{E_s}{1-\nu^2}\partial_1\partial_1 d_1 + \frac{E_s}{2(1+\nu)}\partial_2\partial_2 d_1 \\
&\qquad + \frac{E_s}{2(1-\nu)}\partial_1\partial_2 d_2 = -T_1, \\
&\frac{E_s}{1-\nu^2}\partial_2\partial_2 d_2 + \frac{E_s}{2(1+\nu)}\partial_1\partial_1 d_2 \\
&\qquad + \frac{E_s}{2(1-\nu)}\partial_2\partial_1 d_1 = -T_2.
\end{aligned} \tag{3}$$

In these expressions, $E_s = Eh$ is the surface Young modulus. Although it will usually be a constant for any given film, its actual value must be determined empirically by separate calibration measurements (cf. Studies of Film Rheology, below). This is so because, in addition to having a linear dependence on the membrane thickness, $E_s$ can be a sensitive function of the degree of cross-linking and also of the amount of prestress. Note that, despite the important stabilizing role played by the drumhead tension, this quantity drops out of Eqs. 3. Thus, although $\bar{\sigma}$ is important to prevent deformations normal to the plane of the membrane (i.e., wrinkling), the precise magnitude of this quantity is irrelevant to the in-plane deformation.

For certain boundary conditions and traction distributions, elegant solutions for the fields of displacement that satisfy Eqs. 3 are known (Timoshenko, 1934). For example, if the elastic medium is infinite and if there are simple stress boundary conditions $\sigma_{\alpha\beta} \to \bar{\sigma}\delta_{\alpha\beta}$ as $|\mathbf{x}| \to \infty$, then the

components of the displacement field can be expressed in integral form:

$$d_\alpha(\mathbf{x}) = \frac{1}{E_s}\int\int (g_{\alpha 1})\mathbf{x}, \mathbf{f})T_1(\mathbf{f}) + g_{\alpha 2}(\mathbf{x}, \mathbf{f})T_2(\mathbf{f}))\mathbf{df}, \quad (4)$$

where

$$g_{\alpha\beta} \equiv \frac{(1+\nu)^2}{4\pi}\left[\frac{(x_\alpha - f_\alpha)(x_\beta - f_\beta)}{|\mathbf{x}-\mathbf{f}|^2} + \delta_{\alpha\beta}\frac{(3-\nu)}{(1+\nu)}\ln\left(\frac{1}{|\mathbf{x}-\mathbf{f}|}\right)\right]. \quad (5)$$

Physically, the nondimensional functions $g_{\alpha\beta}(x_1, x_2, f_1, f_2)$ can be thought of as giving the displacement in the $\alpha$ direction at location $(x_1, x_2)$ induced by a delta function traction density acting in the $\beta$ direction at location $(f_1, f_2)$. In other words, the $g_{\alpha\beta}$ are the components of a so-called displacement Green's function. Chapter 5 of the text by Timoshenko (1934) can be consulted for further details.

Substitution of some special choices for the traction density reveals that for many loadings the integral required by Eq. 4 will not exist. Physically this should not be surprising because it is certainly conceivable that under some conditions an unbounded elastic membrane with stress boundary conditions will slip tangentially and undergo an infinite displacement without reaching equilibrium. To avoid such pathology and thereby ensure the existence of the integral in Eq. 4 it is sufficient that the traction density field have bounded support and satisfy a constraint of global force balance:

$$\int\int T_1(\mathbf{f})\,\mathbf{df} = \int\int T_2(\mathbf{f})\mathbf{df} = 0. \quad (6)$$

Fortunately it is easy to see that the traction field generated by a freely locomoting cell, normal to the gravitational field and having no contacts with the external world except through the elastic substrate, will always satisfy Eq. 6. Therefore, in the subsequent discussion we will concentrate strictly on the analysis of such freely locomoting cells. The important generalization to the case of cells locomoting against external loads requires additional work and will be dealt with in a subsequent publication.

## IMAGE ANALYSIS

We now turn to the question of what can be learned about the traction field acting on an elastic film from observations of the displacement field. In the interests of specificity we presume that a digitized image, with pixel resolution $s$, has been obtained to record the centroid location of a finite number of small marker particles embedded in the undisturbed elastic material. We further presume that at some later time a cell wanders into the observation field, causing a small disturbance. The particle locations are then observed for a second time, and for each particle the displacement relative to the undisturbed position is computed with image-processing software. We let $\hat{\mathbf{d}}^p = (\hat{d}_1^p, \hat{d}_2^p)$ and $\mathbf{x}^p = (x_1^p, x_2^p)$ be the resulting experimental measurements of displacement and initial location of the $p$th particle ($p = 1, 2 \cdots P$). Finally, we assume that the theory of the preceding section is applicable, that both $E_s$ and $\nu$ are known, and that the presence of particles in the film does not contribute a significant perturbation to its elastic behavior.

Inasmuch as displacements are computed by subtracting a reference image from a disturbed image, it is naturally very important that the two images share the same origin and orientation with respect to a set of fixed reference markers. The systematic error introduced into the measured displacements by misalignment of the two images is called a "drift correction." If we include both random error and translational drift error, then the observed displacement of the $p$th particle is given as the sum of three vectors:

$$\hat{\mathbf{d}}^p = \mathbf{d}^p + \mathbf{w}^0 + \mathbf{r}^p. \quad (7)$$

Here $\mathbf{d}^p = \mathbf{d}(\mathbf{x}^p)$ is the systematic displacement that would be obtained by a perfect measurement (we could compute this term by using Eq. 4 if we knew the exact traction density field being applied to the substratum by the cell). The second term on the right-hand side of Eq. 7 is the drift correction, and the third term is the random error. In our experience, translational drift is always present and must be carefully accounted for even though the actual size of the misalignment may be only a fraction of a pixel. In principle one could also include a correction for rigid rotation of the reference and the disturbed image with respect to some arbitrary axis. However, until now it seems that this additional correction was not needed, at least if the sample was carefully clamped during the interval that elapses between the reference and disturbed images.

This extreme sensitivity arises because the translational drift is the same for all the particles and therefore introduces a cumulative systematic error that gets progressively worse as the number of particle observations is increased. In contrast to the drift corrections, the $r_\alpha^p$ are independent random numbers that tend to cancel. We will henceforth assume that the $r_\alpha^p$ are all sampled from a single Gaussian distribution. We will further assume that the mean value of this distribution is zero and that the standard deviation is equal to the pixel radius.

### Representing the Set of A Priori Possibilities

To make further progress we now construct a space of finite dimension from which to select candidate traction images. For this purpose it is important formally to recognize the common-sense idea that cells can apply tractions to a substratum only at points where they make some direct contact. This means that in constructing the space of possible traction images it is safe to assume that all the tractions occur within the boundaries of some sharply delimited region, $\Omega$.

Usually but not always $\Omega$ will correspond to the projected image of the locomoting cell. As a second condition on the candidate traction images it is also necessary to eliminate any image violating the constraint of global force balance, Eq. 6.

Aside from such physical constraints, the $T_\alpha$ could conceivably be any continuous functions. To represent this large space of possibilities efficiently we assume that the interior of $\Omega$ is paved by a mesh of quadrilaterals. To interpolate the $T_\alpha$ smoothly over our mesh we then define so-called nodal "shape" functions, $S^k(\mathbf{f})$, all with the usual finite element property of $C_0$ continuity. We also require that each of and all the $S^k$ satisfy the "localization" conditions:

$$S^k(\mathbf{f}^j) = \delta_{kj} \quad \forall j = 1, 2, \cdots \mathrm{N}. \tag{8}$$

In Eq. 8, N is the number of nodes, $\mathbf{f}^j = (f^j_1, f^j_2)$ is the location of the $j$th node, and $\delta_{kj}$ is the Kronecker delta. Finally, the total traction density distribution over the mesh is written as a sum over nodal tractions:

$$\mathbf{T}(\mathbf{f}) = \sum_{k=1}^{\mathrm{N}} \mathbf{w}^k \left( S^k(\mathbf{f}) - \frac{A^k}{A_\mathrm{T}} \right), \qquad \mathbf{f} \in \Omega. \tag{9}$$

Here

$$A_\mathrm{T} \equiv \int\int_\Omega \mathrm{d}\mathbf{f} \tag{10}$$

is the total mesh area;

$$A^k \equiv \int\int_\Omega S^k(\mathbf{f})\, \mathrm{d}\mathbf{f} \tag{11}$$

is the area surrounding the $k$th node. The $\mathbf{w}^k = (w^k_1, w^k_2)$ are the mesh associated degrees of freedom that implicitly encode the descretized traction image. In view of the definition of the $A^k$, one can easily verify by substitution into Eq. 6 that the constraint of global force balance is exactly satisfied by Eq. 9 for any choice of the $\mathbf{w}^k$; $k = 1, \cdots \mathrm{N}$.

In the subsequent development, it simplifies the algebra considerably if we regard the components of the drift correction vector, $\mathbf{w}^0 = (w^0_1, w^0_2)$, as being equivalent to degrees of freedom associated with an imaginary zeroth node of the mesh. Consistency then requires that we define the null area and the null shape function as also being associated with the zeroth node. Accordingly, whenever necessary we will henceforth implicitly assume that it is legitimate for the nodal index to take a value of zero and moreover that $S^0(\mathbf{f}) = 0$ and $A^0 \equiv 0$.

Finally, to avoid any possible confusion, we should take this opportunity to point out that according to Eqs. 9 and 8, the traction density vector at the $n$th mesh node is

$$\mathbf{T}^n \equiv \mathbf{T}(f^n) = \mathbf{w}^m - \sum_{k=1}^{\mathrm{N}} \mathbf{w}^k \frac{A^k}{A_\mathrm{T}} = \mathbf{w}^n = \bar{\mathbf{w}}. \tag{12}$$

Thus, in general, $\mathbf{T}^n \neq \mathbf{w}^n$.

## Bayesian Likelihood of a Hypothesis

Let $\{X\}$ be the set of all possible outcomes of an experiment, and let the particular result $X$ be obtained in practice. A "test hypothesis," $H$, consists of some guess for the unknown information necessary to generate a complete prediction of this experimental outcome. In the current context such a hypothesis consists of a definite choice of the $w^k_\alpha$ for $k = 0$, $1, \cdots \mathrm{N}$ and $\alpha = 1, 2$ (i.e., $2\mathrm{N} + 2$ real numbers). Now, suppose that before conducting our experiment we recorded an estimate of the probability that the test hypothesis is true. Letting $P(H)$ be this initial probability, we will symbolically denote the corresponding quantity after obtaining the experimental result $X$ by $P(H \mid X)$. If $\{H\}$ is the universe of all the theories to be tested, then the hypothesis that affords the best explanation of the experiment is defined by the element of $\{H\}$ that maximizes $P(H \mid X)$.

To compute $P(H \mid X)$ for arbitrary $H$ and $X$ we utilize the well-known rule of inductive logic that is due to Bayes (Bernardo and Smith, 1994). According to this result the postexperimental probability of a hypothesis is expressed as the product of three factors:

$$P(H \mid X) = P(X \mid H) P(H) S_x^{-1}. \tag{13}$$

The first quantity on the right-hand side of Eq. 13 in this equation is interpreted as the probability of obtaining the experimental outcome, $X$, on the assumption that the test hypothesis is true. It is simply common sense to assert that, when this quantity is large, our belief in the underlying hypothesis should increase in a more-or-less proportional fashion. Equation 13 also implies that the postexperiment probability of a test hypothesis will be proportional to the preexperiment probability. Once again this is common sense because, in practice, our opinion of a test hypothesis before an experiment should be only partially modified as the result of a single experimental experience. Finally, the quantity $S_\mathrm{X}$ that appears on the right-hand side of Eq. 13 is just a normalization constant chosen so that the integral of $(P(H \mid X)$ over all $H \in \{H\}$ will be exactly equal to 1.

The probability of a particular experimental outcome, given a test hypothesis, is identical to the probability of obtaining certain actual values of the error vectors by random sampling from an appropriate distribution. In the case of the current experiments, the errors in the particle displacement measurements are assumed to be Gaussian with means of zero and standard deviations equal to the pixel radius. Thus, except for an irrelevant normalization constant, the probability of the observed experiment is

$$P(X \mid H) \propto \exp(-\chi^2), \tag{14}$$

where

$$\chi^2 \equiv \sum_{\mathrm{p}=1}^{\mathrm{P}} \left| \frac{\mathbf{r}^\mathrm{p}}{s} \right|^2 = \frac{1}{s^2} \sum_{\mathrm{p}=1}^{\mathrm{P}} \left| \hat{\mathbf{d}}^\mathrm{p} - \mathbf{w}^0 - \mathbf{d}^\mathrm{p} \right|^2 \tag{15}$$

is the familiar chi-squared statistic.

## A Priori Likelihood of a Traction Image

In view of the fact that the $\mathbf{d}^{\mathrm{p}}$ must be evaluated from Eqs. 4, 5, and 9, actually computing the value of $P(X|H)$ by using Eq. 14 can require considerable mathematical effort. Nevertheless, at least the basic idea of Eq. 14 is unambiguous and objective. In contrast, evaluating the initial probability of a particular test hypothesis constitutes a more slippery and difficult topic. This is because $P(H)$ necessarily embodies various personal beliefs and biases, because these are not usually subjected to objective scrutiny, and because there is in any case no absolute standard to apply.

The classical method to lance rhetorically the subjectivity of a given individual's prior belief is to confront him or her with the imaginary or simulated viewpoints of some small collection of trusted and neutral authorities (hereafter designated $O_1$, $O_2$, etc). After first carefully explaining the biases and virtues of these ideal observers, we will faithfully demonstrate what each observer concludes from any given experiment, and we invite consideration of these conclusions. We then appeal to the empathic facility of our species. If possessed of this ability, an individual should be able to extrapolate from the situation of the imaginary observers and thereby draw his or her own conclusions.

The first and most important characteristic of $O_1$ is that he believes in a form of Occam's principal. By analogy with Eq. 14 this means that he always tries to rank the intrinsic likelihood of images according to the inverse of a positive functional called "complexity":

$$P(H) \propto \exp(-\mathscr{C}^2). \tag{16}$$

The specific definition of complexity used by $O_1$ is as follows;

$$\mathscr{C}^2 = \int_{\Omega} \left(\frac{T_1(f_1, f_2)}{\lambda}\right)^2 + \left(\frac{T_2(f_1, f_2)}{\lambda}\right)^2 \frac{\mathrm{d}f_1\,\mathrm{d}f_2}{A_{\mathrm{tot}}}. \tag{17}$$

According to this definition, the image of minimum complexity is the trivial or null image wherein the traction density is everywhere exactly equal to 0. Other images are then ranked according to the average magnitude (or $L_2$ norm) of the traction density. Readers who think that this definition of complexity is not to their liking are advised to have patience; we will subsequently consider an alternative definition.

The quantity $\lambda$, hereafter called the "complexity scale," is a positive real number with the same dimensions as the traction density. In essence $\lambda$ is just $O_1$'s a priori "order-of-magnitude" estimate of the rms traction density of the minimal field that can be expected to produce a detectable effect on the particles under observation. An astute computation of the required quantity can be derived from a dimensional analysis:

$$\left[\frac{E_s s}{\lambda}\right]^2 \tag{18}$$

$$= \sum_{m=1}^{N} \sum_{p=1}^{P} \frac{N}{2P} \sum_{\alpha=1}^{2} \sum_{\beta=1}^{2} \left[\iint g_{\alpha\beta}(\mathbf{x}^{\mathrm{p}}, \mathbf{f}) \left(S^m(\mathbf{f}) - \frac{A^{\mathrm{m}}}{A_{\mathrm{T}}}\right) \mathbf{df}\right]^2.$$

The final traction image obtained by maximizing $P(H|X)$ by using Eq. 18 in conjunction with Eq. 17 in the maximum-likelihood hypothesis according to $O_1$. Note that according to Eq. 18 $\lambda$ depends on the mesh geometry and also on the undisturbed locations of the beads or particles being observed. The complexity scale does not depend on the actual motions of the beads and is thus a true a priori estimate. Subsequently we will apply Monte Carlo techniques to study the characteristic errors and biases of $O_1$'s maximum-likelihood image (see Statistical Studies, below).

## A Second Opinion

We will from time to time have cause to consult the opinion of a second virtual observer, $O_2$. We will assume that this second observer also believes in Occam's principal but that he differs from $O_1$ in that he assigns special importance to derivatives of traction magnitude and direction. $O_2$ also insists that complexity should be a scalar invariant and thus independent of the choice of coordinate system. The alternative viewpoint of $O_2$ then leads to the following mathematical definition:

$$\mathscr{C}^2 = \int_{\Omega} 2\left(\frac{\partial_1 T_1}{4\lambda}\right)^2 + \left(\frac{\partial_2 T_1 + \partial_1 T_2}{4\lambda}\right)^2 + 2\left(\frac{\partial_2 T_2}{4\lambda}\right)^2 \mathrm{d}f_1\,\mathrm{d}f_2. \tag{19}$$

Note that $O_2$'s concept of complexity employs the same scale parameter as $O_1$'s definition. In addition, both $O_1$ and $O_2$ agree that the uniform or null image is the image of minimum complexity. Nevertheless the basic ranking of image complexity used by $O_2$ is fundamentally different from that used by $O_1$. Thus at least to some extent these two observers are independent of each other.

## Computational Details

The main computational effort involved in computing a traction map is expended to find the element of $\{H\}$ that maximizes $P(H|X) = P(X|H)\,P(H)$ for given data, given mesh, and given value of $\lambda$. Substituting Eq. 9 into Eq. 4 and using Eq. 7, we see that for any choice of the degrees of freedom the random error of the observed displacement of the $p$th particle in the $\alpha$th direction can be given as a linear combination of node vectors:

$$r_\alpha^{\mathrm{p}} = \hat{\mathrm{d}}_\alpha^{\mathrm{p}} - \sum_{m=0}^{N} \sum_{\beta=1}^{2} \xi_{\alpha\beta}^{\mathrm{pm}} w_\beta^{\mathrm{m}}. \tag{20}$$

We substitute into Eq. 15, the chi-squared statistic for a discretized traction image takes the form

$$\chi^2 = \sum_{p=1}^{P} \left| \frac{\mathbf{r}^p}{s} \right|^2 = \frac{1}{s^2} \sum_{p=1}^{P} \sum_{\alpha=1}^{2} \left| \hat{d}_\alpha^p - \sum_{m=0}^{N} \sum_{\beta=1}^{2} \xi_{\alpha\beta}^{pm} w_\beta^m \right|^2. \quad (21)$$

In view of the nature of the drift correction terms, it is easily verified that for all particles the coupling coefficients to the zeroth node are

$$\xi_{\alpha\beta}^{p0} = \delta_{\alpha\beta}.$$

For other nodes, the coupling coefficients can be computed by integration:

$$\xi_{\alpha\beta}^{pm} \equiv \frac{1}{E_s} \int_\Omega g_{\alpha\beta}(x_1^p, x_2^p, f_1, f_2) \left( S^m(f_1, f_2) - \frac{A^m}{A_T} \right) df_1\, df_2.$$

Generally we approximate the indicated integrals in the standard way for finite elements by sums over the Gauss points of the mesh quadrilaterals. The only subtlety arises in the special case of a particle located very close to one of the Gauss points. In this situation a simple analytic expression is used to estimate the small contribution arising from a neighborhood surrounding the singularity of the Green's function.

Using Eq. 17 together with Eq. 9, we find that for a discrete image the complexity $O_1$ can be written in the form of a finite sum:

$$\mathcal{C}^2 = \lambda^{-2} \sum_{k=0}^{N} \sum_{m=0}^{N} \sum_{\alpha=1}^{2} d_\alpha^k w_\alpha^m \zeta^{km}. \quad (22)$$

Moreover, the coefficients of this sum are constants that depend only on the mesh geometry:

$$\zeta^{km} \equiv \left[ \int_\Omega S^k(\mathbf{f}) S^m(\mathbf{f}) \frac{df_1\, df_2}{A_{tot}} \right] - \left[ \frac{A^k A^m}{A_{tot}^2} \right]. \quad (23)$$

Once again the indicated integrals can be computed numerically.

Plugging Eq. 20 into Eq. 14 and combining the result with Eq. 16 and Eq. 17, we obtain the postexperiment likelihood of an arbitrary test hypothesis in terms of its underlying degrees of freedom. Then, taking the logarithm and differentiating with respect to $w_\alpha^k$, we obtain 2 N + 2 simultaneous linear algebraic equations:

$$\lambda^{-2} \sum_{m=0}^{N} \zeta^{km} w_\alpha^m - s^{-2} \sum_{p=1}^{P} \sum_{\beta=1}^{2} \xi_{\beta\alpha}^{pk} \left( \hat{d}_\beta^p - \sum_{m=0}^{N} \sum_{\gamma=1}^{2} \xi_{\beta\gamma}^{pm} w_\gamma^m \right) = 0. \quad (24)$$

Some tedious algebra coverts these equations into standard matrix format:

$$\sum_{m=0}^{N} \sum_{\beta=1}^{2} B_{\alpha\beta}^{km} w_\beta^m = b_\alpha^k,$$

where

$$B_{\alpha\beta}^{km} \equiv \lambda^{-2} \zeta^{km} \delta_{\alpha\beta} + s^{-2} \sum_{p=1}^{P} (\xi_{1\alpha}^{pk} \xi_{1\beta}^{pm} + \xi_{2\alpha}^{pk} \xi_{2\beta}^{pm}),$$

$$b_\alpha^k \equiv s^{-2} \sum_{p=1}^{P} \xi_{1\alpha}^{pk} \hat{d}_1^p + \xi_{2\alpha}^{pk} \hat{d}_2^p.$$

Once the $w_\beta^m$ that satisfy Eq. 24 are computed, it is a simple matter to construct the maximum-likelihood traction image by backsubstitution into Eq. 9. The procedure for computing $O_2$'s prediction of the traction image is entirely similar, except that the $\zeta^{km}$ must be modified.

We accomplished the necessary linear algebra to solve Eq. 24 using LU decomposition (described by Press et al., 1989). Most calculations were carried out by 32-bit arithmetic, but spot checks with 64-bit arithmetic revealed no significant problems with roundoff errors. We should caution, however, that in the current study no meshes with more than 256 nodes were used. For meshes involving more than 256 nodes, it might be necessary to develop iterative refinement procedures.

## STATISTICAL STUDIES

Fig. 1 *A* shows the typical use of a quadrilateral mesh to describe the projected region of cell-to-substratum contact. The direction and magnitude of the traction density field acting at the center of each mesh quadrilateral are indicated by an arrow. The traction pattern described by these arrows was chosen at random from a large sample of independent possibilities. Thus, although the traction density field of Fig. 1 *A* satisfies the necessary constraint of global force balance, it is otherwise fictional and any resemblance to the actual traction pattern generated by a real cell, living or dead, is coincidental. Furthermore, we remind the reader that, although the traction density field is necessarily indicated by arrows only at a small number of strategic locations, it is actuality continuous and smoothly changing over the entire mesh interior (see Eq. 9).

Starting with the traction field of Fig. 1 *A*, and assuming that the surface Young's modulus is known, one can proceed to compute the exact displacement of the elastic film at any desired position by using Eq. 4. Such a calculation, for $E_s = 10^4$ dyn/cm at 103 randomly selected test locations, is shown in Fig. 1 *B*. This choice of Young's modulus suffices because it is apparent from the form of Eq. 4 that changing the surface Young modulus will simply cause an inversely proportional correction in the magnitudes of all the displacement vectors. The base of each arrow in Fig. 1 *B* corresponds to the location of one of the test locations in the undisturbed or reference state of the film. The length and direction of the arrows then indicate the motion that a particle at this initial location undergoes after application of the traction field. Note that for greater visibility these dis-

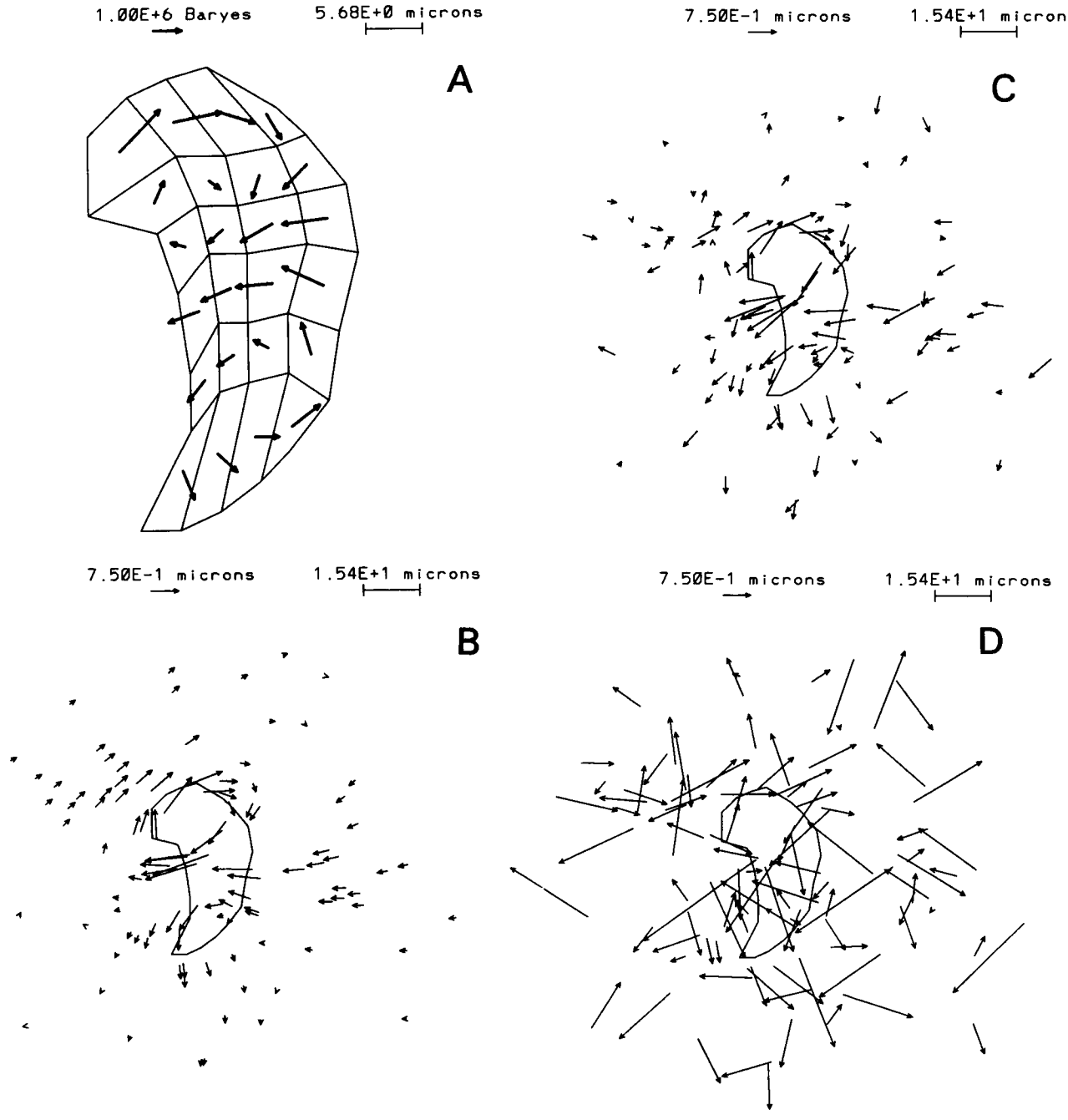


FIGURE 1 Computation of the displacement field. (*A*) Typical use of a quadrilateral mesh to describe a contact region, $\Omega$, and the associated traction density field. The scale factors for traction vectors and position vectors are indicated by the labeled arrow and the distance bar at the top of the figure. Note that the scale for traction stress is expressed in cgs units (Barye $\equiv$ 1 dyn/cm$^2$). The illustrated stress field is purely hypothetical, although it has certain characteristics of real traction density fields (i.e., the field is smoothly varying and satisfies the constraint of global force balance). (*B*) The theoretical displacement caused by the hypothetical traction density field of (*A*) at 103 randomly selected locations. Displacement computations were carried out using Eq. 4 and assuming $E_s = 10^4$ dyn/cm. Displacement vectors in this and other figures are not actual size but are magnified for better visibility (see the reference arrow). (*C*) Same data as in (*B*), except that experimental error has been simulated by addition of a drift error plus a random error to each of the displacement vectors. The signal-to-noise ratio in this Monte Carlo simulation is 5:1. (*D*) Same as (*C*), except that the simulated signal-to-noise ratio is now 1:1.

placement vectors are exaggerated relative to the actual particle motion. In this and other figures the magnification factors are indicated by a labeled reference vector near the top of the figure. Note that, although the displacement field is indicated by arrows only at the selected test locations, it is actually continuous, just like the traction vectors. Unlike the traction field, however, the displacement field extends smoothly over the entire infinite area of the elastic medium and is not strictly confined to the region of cell–substrate contact.

The mesh of Fig. 1 *A* and also the general distribution and number of "particles" in Fig. 1 *B* are typical of what is encountered in actual experiments. However, in a real experiment the orderly field of displacements as shown in Fig. 1 *B* would be partially masked owing to drift error and measurement error. To obtain a more realistic rendering of what is actually seen experimentally one must therefore superimpose appropriate error terms upon the exact particle displacements. The typical result of such processing for two levels of noise is indicated in Fig. 1 *C* and *D*. To illustrate a worst-case situation we have taken the standard deviation of the noise ratio in the second of these simulations to be equal to the maximum systematic particle displacement. Such large error would occur only in an experiment in which the true displacement of particles was less than the pixel spacing. In any event the signal-to-noise ratio is such that the unaided eye has difficulty in seeing any remnant of the underlying systematic pattern.

Generally, a simulation of particle displacements that is realistic even to the point of including random noise, random drift error, and a random distribution of particle locations can be called a Monte Carlo simulation. Fig. 1 *C* and *D* shows examples of Monte Carlo simulations in which it is assumed that a cell characterized by a certain "test" shape is exerting a certain "test" traction field upon the substratum (i.e., the field of Fig. 1 *A*). More generally, any traction pattern and cell shape could be used as the basis for constructing a Monte Carlo simulation. If the Monte Carlo simulation of displacement data is correctly conducted, its outward appearance very much resembles the result of a real experiment. In particular, the ideal observers $O_1$ and $O_2$ have no way of telling the difference between a simulated experiment and a real experiment. Consequently, Monte Carlo simulations can be used to conduct objective trials of the accuracy of the reconstructed traction images produced by the ideal observers.

In a typical Monte Carlo trial we confront an observer with the noisy displacement field resulting from a simulation and obtain his or her best opinion as to the underlying traction field. We then compare this reconstructed field with the test traction field known only to us. Systematic repetitions of this procedure can in principle provide answers to a host of detailed statistical questions. For example, we can determine how sensitive a reconstructed traction image is to the test mesh, to the signal-to-noise ratio of the simulated data, to the number and distribution of particles, to prior bias of the observer, to characteristics of the underlying test traction field, etc.

Fig. 2 *A* and *B* shows the results obtained when $O_1$ attempts to construct a traction image starting with the Monte Carlo simulations shown in Fig. 1 *C* and *D*, respectively. Fig. 2 *C* and *D* shows the analogous results obtained when the simulated data are processed by $O_2$. Comparison of the reconstructed images with the exact traction field (given in Fig. 1 *A*), allows one to determine the accuracy of the reconstructions. Obviously, in this example neither observer gets a perfect score, but in general most features of the exact images are recognizable in the reconstructions. We are thus partially reassured that both $O_1$ and $O_2$ can reconstruct useful approximations of the particular test traction image used for this example even if the displacement observations are few and of low accuracy. The inevitable degradation of the quality of the reconstructed image that is due to the noise level of the data can be seen by comparison of Fig. 2 *A* and *B* and likewise of Fig. 2 *C* and *D*. Comparison of Fig. 2 *A* and *B* and likewise of Fig. 2 *B* and *D* reveals that $O_1$ and $O_2$ produce very similar results. This was a consistent finding in a large spectrum of tests.

Monte Carlo simulations can be used to illustrate the consequences of introducing modifications into the definition of complexity scale used by an ideal observer. For example, in Fig. 3 *A* we show what happens to the image deduced by $O_1$ if we decrease the standard value of $\lambda$ by a factor of 2. The effect is to cause the observer to place less reliance on the data at hand and more reliance on his preconceived notions of complexity. The final maximum-likelihood image deduced by $O_1$ is thus overly conservative or skeptical (compare Figs. 3 *A*, 2 *B*, and 1 *A*). In other words, if the retained features of the reconstructed traction image are real but the magnitudes are too low some of the more interesting details of the test traction image are lost.

In contrast, the effect of increasing the complexity scale by a factor of 2 is shown in Fig. 3 *B*. As a result of this modification $O_1$ places more emphasis on the particular noisy data at hand and less reliance on his preconceived notions. As a result he tries to extract too much information from a single noisy data set and in effect fails to filter adequately the signal from noise. The end product, Fig. 3 *B*, is an overly liberal image in which many features are the result of noise and are not strongly necessitated by the data.

We should emphasize that the results of Fig. 3 *A* and *B* correspond to relatively modest changes in the choice of complexity scale. Thus these images, though they are not optimal, might still be acceptable for some applications. If $\lambda$ is increased or decreased by even larger amounts, (say, by a factors of 10 or more), then the quality of the reconstructed images will be very poor and virtually useless (data not shown). In particular, disastrous results ensue if we let all images in $\{H\}$ have equal a priori likelihood (equivalent to setting $\lambda = \infty$).

In addition to the trials indicated in Figs. 2 and 3 we have carried out many hundreds of independent Monte Carlo tests, using a battery of different meshes of various sizes and shapes. For each mesh we have tested the ability of both $O_1$ and $O_2$ to reconstruct 10 different traction density patterns spanning the broad range of possibilities. Simulations also involved different choices for the number of observed particles and different choices for the random distribution of these particles with respect to the mesh centroid. Finally, we simulated data by using several different signal-to-noise ratios. The voluminous results are best summarized by simply stating that both $O_1$ and $O_2$ give accurate reconstructions even of complex traction images and even with very noisy data. In all but a few extreme cases the tractions

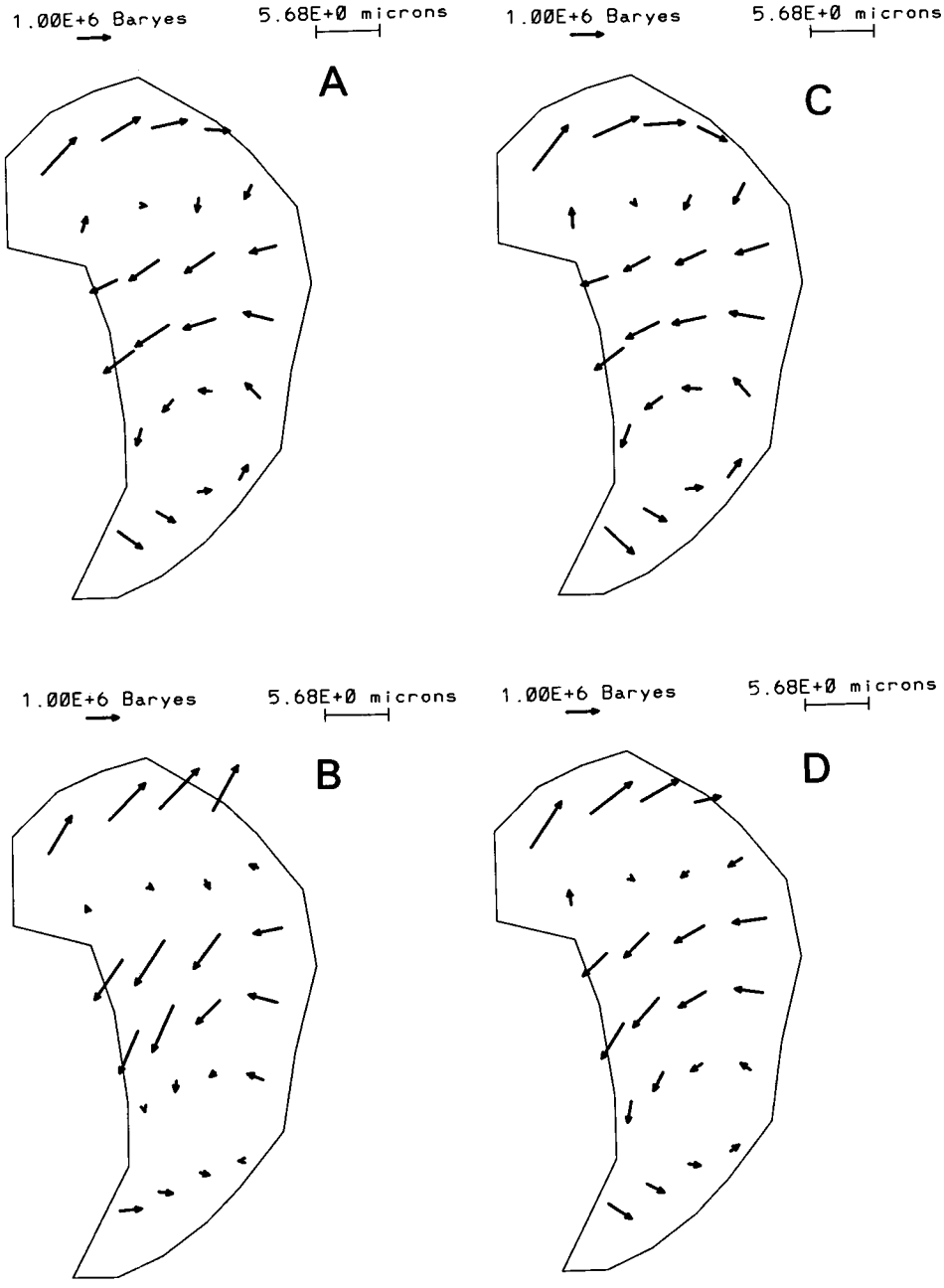


FIGURE 2 Effect of noise level and observer on reconstructed traction images. (*A*) Traction field reconstructed by $O_1$ based on the low noise simulation of Fig. 1 *C*). (*B*) Traction field reconstructed by $O_1$ based on the high noise simulation of Fig. 1 *D*. (*C*) Traction field reconstructed by $O_2$ based on the low noise simulation of Fig. 1 *C*. (*D*) Traction field reconstructed by $O_2$ based on the high noise simulation of Fig. 1 *D*.

images of $O_1$ and $O_2$ are very similar and conservative; they systematically underestimate the extremes of traction magnitude, and they overestimate the degree of alignment of the traction field.

From Monte Carlo simulations it is clear that the best images are obtained when the displacement vectors are scattered randomly throughout a circular field with diameter extending well beyond the boundaries of the mesh. Asymmetric distributions of the bead positions tend to introduce bias into the results. The characteristic diameter of the particle distribution should be at least twice as large as the diameter of the mesh. Apparently, this is so because observations far from the cell provide valuable reference markers needed for accurate drift corrections and for the lower moments of the traction field. Displacement measurements at points directly under the cell yield more detailed "local" information. Small "features" or details of a traction image will tend to be lost in the reconstructed image unless the characteristic size of the feature is larger than the average spacing between particles in the field.

Simulations also indicate that certain common-sense rules concerning the mesh are valid. For example, the mesh must have sufficient spacial resolution and degrees of freedom to represent the traction field adequately. Further refinement of the mesh beyond this point has little effect on the results. In all cases an accurate but minimal representation of the cell–substratum contact region is most advisable. It is particularly damaging if $\Omega$ is deliberately expanded to

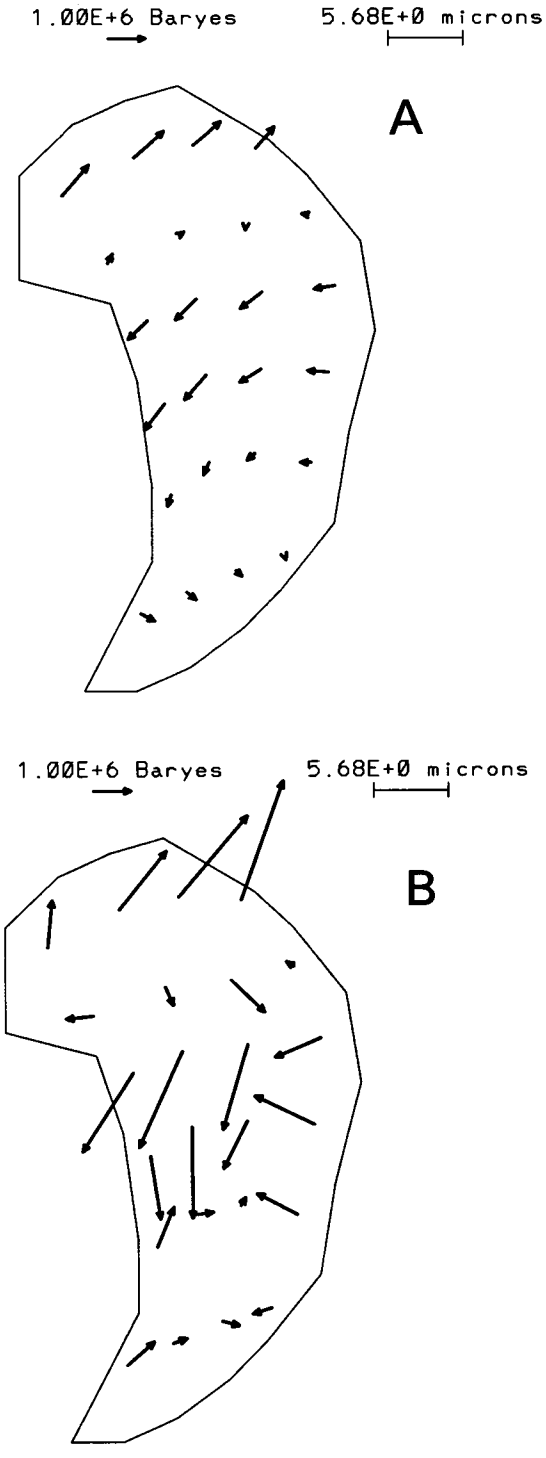


FIGURE 3 Effects of changing the complexity scale on the traction images of $O_1$. (*A*) $\lambda$ is decreased by a factor of 2 relative to the standard value derived from Eq. 18. The qualitative effect is to reduce the complexity of the final maximum-likelihood traction field. The resulting image is usually too conservative in the sense that certain interesting and valid details of the exact traction pattern are omitted. (*B*) $\lambda$ is increased by a factor of 2 relative to the standard value derived by Eq. 18. The qualitative effect is to increase the complexity of the final maximum-likelihood traction field. This can sometimes result in an improved image and a better (lower) value of $\mathcal{X}^2$. Unfortunately the image is usually overly liberal, and there is a danger that spurious features, not well supported by the data, will be present.

include regions where tractions would normally be excluded. This kind of misrepresentation is leveraged by the built-in conservative tendencies of both $O_1$ and $O_2$. As a result the final images will include spurious tractions extending into the areas where they should be forbidden.

## STUDIES OF FILM RHEOLOGY

Manipulation with calibrated microneedles was previously been used to evaluate the suitability of various types of film for use as biological substrata (see Lee et al., 1994; Oliver et al., 1995). These studies demonstrated that film rheology is generally quite sensitive to the detailed conditions of manufacture, particularly the duration of the treatment with glow discharge. Nevertheless, conditions can be controlled to reproducibly generate so-called "elastic" films. When a tangential force is applied at the center of the Rappaport chamber supporting this kind of film, it undergoes an equilibrium displacement by an amount linear in the force (the empirical film stiffness is $\sim$2 mdyn/$\mu$m). Moreover, when the force is removed, films of the elastic type recoil to their initial state with a half-time of $\sim$1 s. Because the displacements caused by needle manipulation in these simple compliance experiments (tens of micrometers) far exceeded the typical bead displacements caused by cells (1/2 $\mu$m), it seems fair to conclude that our so-called elastic films will retain their desirable properties during the time required for measurements of cell-generated tractions.

A difficulty with single-needle compliance studies is that the traction field does not satisfy the condition of global force balance. As a result, the measured compliance of the film by this technique is not a strictly intensive property; it depends on the exact size and shape of the Rapaport chamber and also on the exact placing of the needle within the boundaries of the chamber. To overcome these objections we have devised a new type of experiment in which the film is simultaneously manipulated with two calibrated microneedles configured so as to apply a symmetric "pinching" traction pattern. Such a pattern is consistent with global force balance, and moreover the magnitude of the net traction applied by each needle separately is readily determined. Thus a pinch experiment allows a direct test of the basic integral transform connecting tractions and displacements (Eq. 4). In addition, the pinch experiment can be used to obtain an accurate and unambiguous value for the surface Young modulus of a silicone membrane.

Fig. 4 *A* shows the results of a typical pinch experiment. Two needles of approximately equal stiffness were applied close to the center of an elastic film (square boxes show the initial locations of the microneedle tips). The arrows in Fig. 4 *A* show the observed displacements of marker particles fixed in the film when the needle tips were moved toward each other to reduce the initial separation distance by $\sim$10%. The pinching of the film simultaneously caused the needles to bend slightly. As the needles were calibrated in advance, the magnitude of this bending can be used to

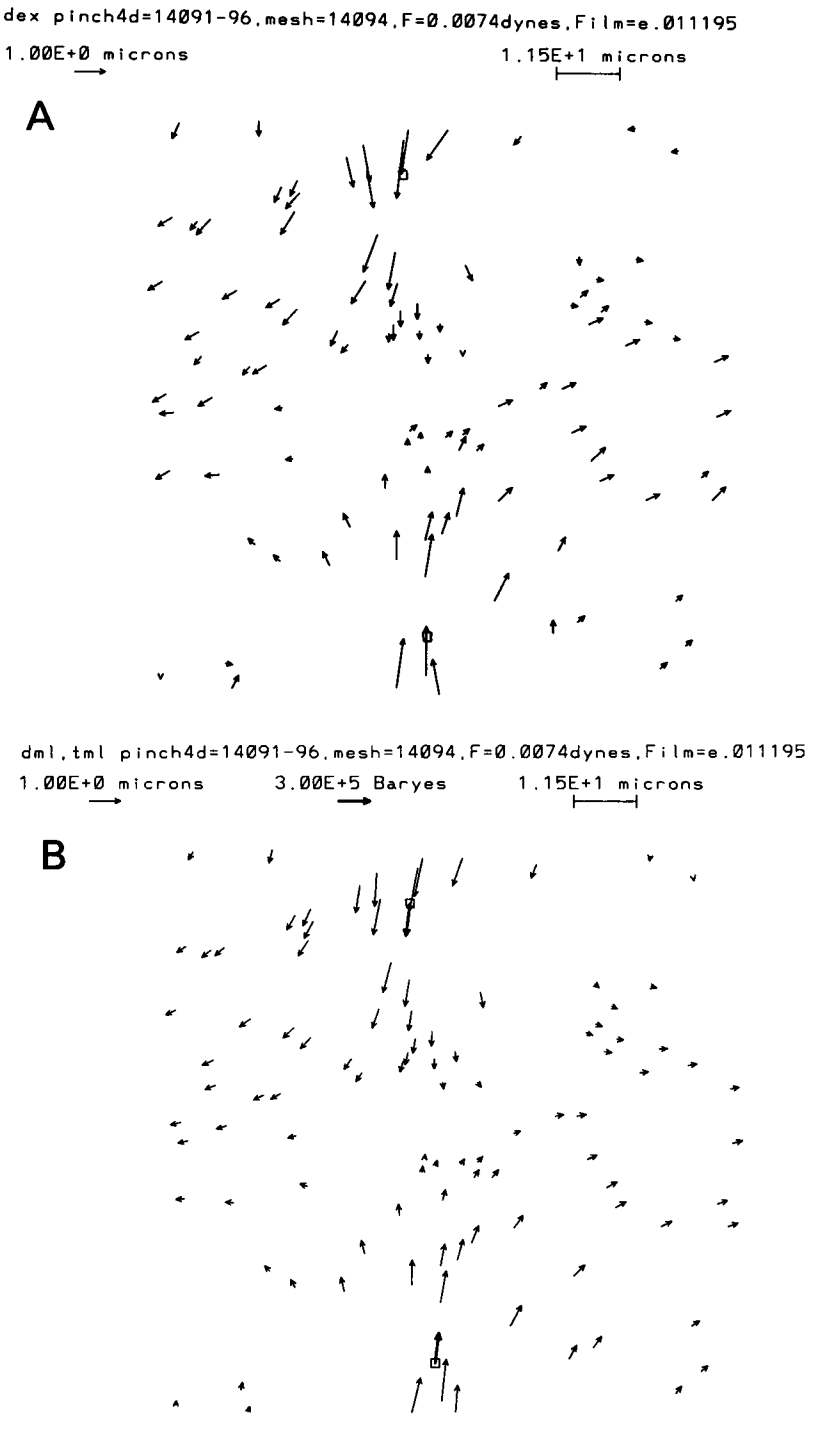


FIGURE 4 Typical "pinch" experiment. (*A*) Two microneedles of approximately equal stiffness are placed in contact with the elastic surface at the locations indicated by the square boxes. The needles are then moved toward each other in a pinching motion to reduce the initial separation distance between them by ~10%. The resulting displacements of 101 marker beads scattered in the vicinity are indicated by arrows. The base of each arrow corresponds to the initial location of a bead; the magnitude and direction then indicate bead displacement in the usual way. The magnitude of the total traction force exerted by the top and bottom needles was independently determined by observation of the extent of needle bending. This force was the same for both needles (7.4 mdyn). (*B*) Maximum-likelihood traction field (thick arrows) and corresponding displacement field (thin arrows) obtained from analysis of the experiment of (*A*). To compute displacements, the force of a needle was assumed to be applied as a uniform traction stress over the box representing its region of contact with the film. The magnitude of the total force of a single needle was fixed at 7.4 mdynes, and the sum of the forces of the two needles together was assumed to be zero (i.e., global force balance was enforced). Finally, after these constraints, the angular direction of the opposed pinching tractions, the surface Young modulus and the drift corrections were determined by data fitting (four free parameters).

determine the exact force being exerted. In the case of Fig. 4 *A* the magnitude of the force by this method (7.4 mdyn) was the same for both needles to within experimental error. This confirms that the pinch was in fact symmetrical and that global force balance is valid.

Fig. 4 *B* shows the theoretical displacement field (thin arrows) predicted by Eq. 4 on the basis of the indicated tractions (thick arrows) applied uniformly across the needle tips. In obtaining the theoretical traction vectors we fixed the product of the traction density and the box area (i.e., the integrated traction force applied by each mironeedle) at the experimental value of 7.4 mdyn. The surface Young modulus, the precise angular orientation of the tractions, and also the drift correction were adjusted to minimize the discrepancy between theory and experiment. The maximum-likelihood value for $E_s$ was 40.9 dyn/cm.

It is clear by inspection of Fig. 4 *A* and *B* that there is general qualitative agreement between theory and experiment, but it is also clear that there are significant differences. Quantitative comparison of Fig. 4 *A* and *B* indicates

a rms difference between corresponding components of the theoretical and experimental displacement vectors of ±0.18 μm (average of 101 beads). For comparison with this quantity one should consider the rms magnitude of the bead displacements themselves (0.65 μm), the wavelength of visible light (~0.5 μm) and also the pixel resolution (±0.12 μm). By all these measures, our general conclusion is that the results of applying defined pinching tractions to elastic-type substrata are reasonably consistent with the corresponding Green's function solutions of the governing equations of small strain-plane stress elasticity. We should emphasize, however, that the theory of small strain-plane stress elasticity is an idealized representation of reality that is only approximately valid. The importance of this can be seem from the results of a test for spatial correlations of the displacement errors (data not shown). Such a test revealed that the errors of the computed displacement field of Fig. 4 *B* tended to be larger closest to the needle tips. Some possible sources of such correlations include 1) indentation of the film owing to the normal forces applied when the needles touch and "grip" the surface, 2) imbalance in the tangential forces applied by the two needles, 3) failure of the small-strain assumption in the case of particles located very close to the needle tips, and 4) error in the placement of the boxes representing the needle tips owing to slippage when the tractions were applied.

In five repetitions, the surface Young modulus of our standard elastic film preparation by the pinch technique was found to be 54 ± 15 dyn/cm. This value was approximately double the empirical stiffness parameter of the standard elastic film as measured in single-needle compliance experiments described previously (see Oliver et al., 1995). This correction factor should be a constant, at least if the single-needle manipulation is always carried out in exactly the same geometry. Thus, when properly corrected, the single needle method can be used as a quick and simple means of determining the surface Young modulus of elastic films.

## ILLUSTRATIVE TRACTION MAP

In a separate publication we recently presented an initial image of the traction pattern exerted upon a substratum by a moving keratocyte (Oliver et al., 1995). Unfortunately, at the time when this first traction image was assembled reliable data on the surface Young modulus of the standard elastic film were not yet available. This meant that only the direction and relative magnitude of traction stresses at various positions under the cell could be obtained. The newly available values of $E_s$ (see the pinch experiments described above) now make it feasible to report fully calibrated images in which traction stresses are given in absolute physical units. In addition to obtaining such calibrated images it is also instructive to dwell on some of the biophysical nuances and ambiguities that can result from changes in the underlying statistical processing of displacement data. Details of the experimental approaches used for preparation of keratocytes, for preparation of elastic films, and for collection and recording of data on bead displacements and cell shape were all described previously (Oliver et al., 1995; Lee et al., 1994).

Fig. 5 *A* shows the mesh representation of the image of a typical keratocyte moving in a straight path toward the positive Y direction on a standard elastic film. The total area of the cell–substratum contact defined by the interior of this mesh is 656 $\mu m^2$. Experimental observations of particle displacements ($n = 95$) in the field surrounding the moving cell are shown by arrows. Fig. 5 *B* shows the traction density field reconstructed by $O_1$ based on these data. The corresponding reconstruction by $O_2$ is shown in Fig. 5 *C*. The tractions of Fig. 5 *B* and *C* are fully calibrated based on the best available estimate of $E_s$ for our standard elastic film preparation (see above).

Comparison of Fig. 5 *B* and *C* shows that the conclusions of $O_1$ and $O_2$ are very similar both qualitatively and quantitatively. The virtual observers report tractions applied beneath the cell in a symmetric, pincerlike pattern, and orthogonal to the direction of locomotion. Traction densities are strongest at the two lateral margins of the cell. They diminish and approach zero at the cell center. A consistent pattern of tractions acting in a rearward direction appears just behind the nucleus (more obvious in the case of $O_1$ than in the case of $O_2$). Relative traction densities at the center front of the lamella were small and oriented somewhat randomly, so it is difficult to interpret them with confidence. In the case of $O_1$ the lateral front edges of the cell are characterized by forward-directed traction densities ($O_2$ does not report this feature at this mesh resolution). No forward-directed tractions were observed at the rear of the cell. Because the traction fields of Fig. 5 *B* and *C* are calibrated, we are able to compute some interesting descriptive statistics. For example, the rms average of the cell–substratum tangential stress in both images is $2.2 \times 10^3$ dyn/cm$^2$.

Fig. 5 *D* shows the theoretically predicted displacements of the particles computed with Eq. 4 in conjunction with the maximum-likelihood image of $O_1$. The rms error between theoretical displacement vectors in Fig. 5 *D* and the experimental vectors in Fig. 5 *A* is ±0.094 μm. For comparison the pixel resolution at the magnification used in this experiment is ±0.092 μm. Thus the fit between theory and experiment in the case of this locomoting cell is very close to the theoretical limit of the optics. In addition, we could detect no spatial correlations of either the directions or the magnitudes of the error vectors (data not shown). We should emphasis that, in our hands, this excellent fit between theory and experiment is quite typical.

To check a traction image for error caused by inadequate mesh resolution it is necessary only to repeat the entire calculation, using a refined or modified mesh. Thus Fig. 6 *A* and *B* shows images that are matched in all ways with those of Fig. 5 *B* and *C*, except that each element of the starting mesh has been subdivided into four. Comparison of these two image sets demonstrates that the doubling of spatial

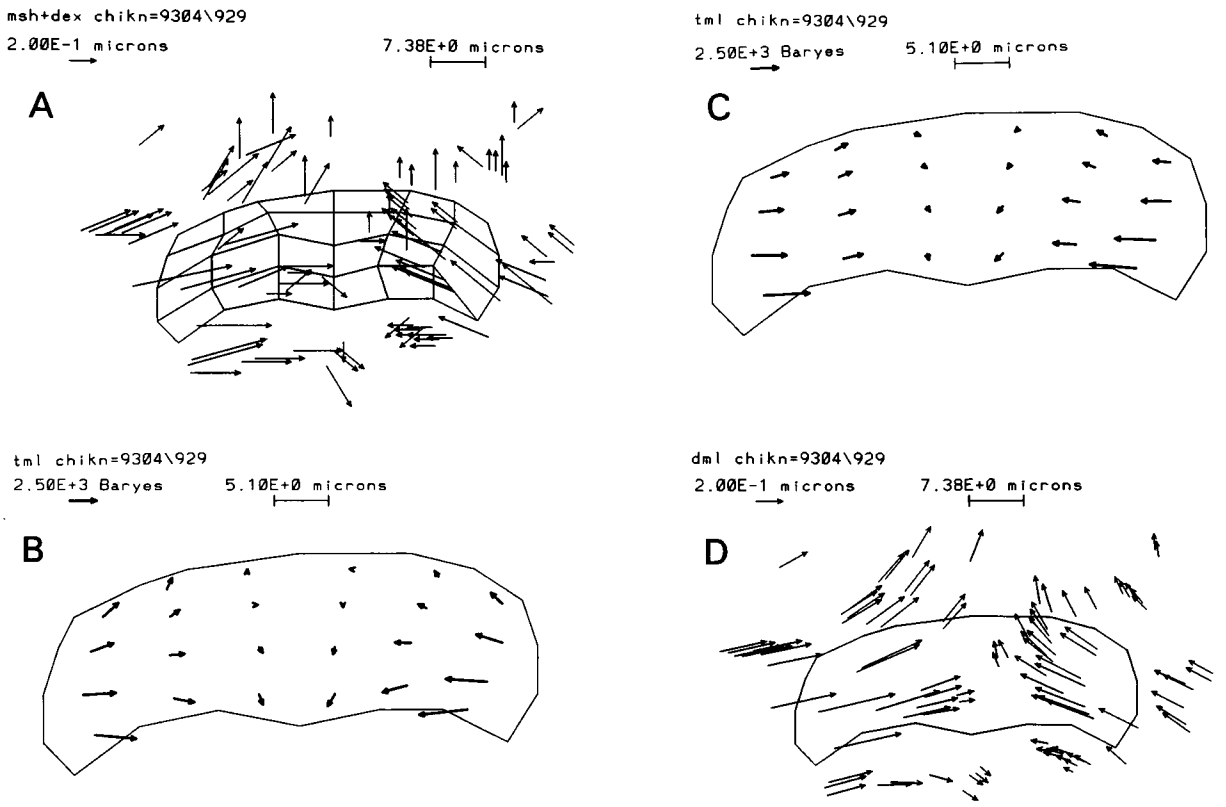


FIGURE 5 Traction image of a locomoting keratocyte. (*A*) Mesh of 24 quadrilaterals defining the domain of the cell–substratum contact for a fish epidermal keratocyte locomoting on the standard elastic silicone rubber film (see Oliver et al., (1995) for details of the experimental methodology). Observations of bead displacement are shown by arrows both inside and outside the domain of cell–substratum contact ($n$ = 95). The reference for undisturbed bead location was taken from analysis of the same location on the film several seconds before the cell appeared in view. The cell is moving in the upward direction at approximately 0.3 $\mu$m/s. The area of the cell–substratum contact is 656 $\mu m^2$. (*B*) Maximum-likelihood traction image reconstructed by virtual observer $O_1$ based on the data and mesh of (*A*). As previously, the scale for traction stress is expressed in cgs units; (Barye ≡ 1 dyn/cm$^2$). (*C*) Maximum-likelihood traction image reconstructed by virtual observer $O_2$ based on the data and mesh of (*A*). (*D*) Bead displacements computed according to Eq. 4 based on the maximum-likelihood traction image of $O_1$. The rms discrepancy between these theoretically predicted displacements and the displacements actually observed (*A*) was ±0.093 $\mu$m.

resolution and the quadrupling of the number of degrees of freedom had rather small consequences. For example, the area average rms traction magnitude was computed as 2.9 ± $10^3$ dyn/cm$^2$ for the image based on a mesh with 96 elements and at 2.2 × $10^3$ for a low-resolution image. As another example, the rms error of the predicted and observed bead displacements was ±0.083 $\mu$m for the mesh with 96 elements and ±0.094 $\mu$m for the mesh with only 24 elements. Despite the basic similarity of high-resolution images to the low-resolution images, some minor issues can be clarified by using high resolution. Thus, in Fig. 6 *A* and *B*, $O_2$ and $O_1$ are seen to agree with respect to the existence of forward-directed tractions at the anterior lateral margins of the cell and also with regard to the rearward-directed traction at the posterior margin.

A traction image is subject to uncertainty resulting from the inherent randomness of the data in addition to error resulting from inadequate mesh resolution. Such uncertainty is usually not uniformly distributed throughout a traction image. Rather it tends to be more or less severe at different locations, depending on the nature of the image itself and on details of particle distribution and cell shape. Despite this potential complexity, it is possible to determine robustly point-by-point error bounds on a traction map by using a parametric bootstrap method (Efron and Tibshirani, 1986). In our implementation we start with known maximum-likelihood traction stress components $T_\alpha^k = T_\alpha(f_1^k, f_2^k)$ at the $k$th mesh node that result from the fitting of a particular experiment. In the end we obtain the corresponding nodal standard deviation components, $\delta T_\alpha^k = \delta T_\alpha^k(f_1^k, f_2^k)$.

We start the necessary procedure by computing maximum-likelihood bead displacements, using the $T_\alpha^k$ and Eq. 4. We then generate 10 independent Monte Carlo simulations. In each of these simulations the undisturbed locations of the beads are exactly as in the experiment, but the disturbed bead location consists of the initial location plus the maximum-likelihood displacement vector, plus independent random motions in the $X$ and $Y$ components, plus drift error. The variance of the random noise in these simulations is fixed in accord with the chi-squared statistic of the original maximum-likelihood fit. The drift error is nominally chosen with a standard deviation of ±1 $\mu$m, which is

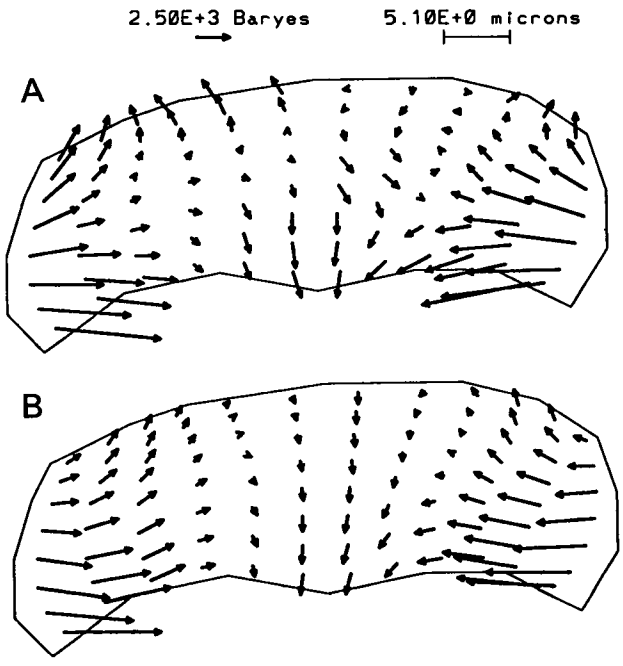


FIGURE 6 Effect of mesh refinement on keratocyte traction images. (*A*) Image of $O_1$. The mesh shown in Fig. 5 *A* was refined by simply dividing each quadrilateral of the original mesh into four. The maximum-likelihood image was then recomputed according to the method of $O_1$ and displayed in the usual way (compare with Fig. 5 *B*). Some improved resolution of the maxima of the traction field is evident, but the basic qualitative and quantitative features are changed little. (*B*) Image of $O_2$. Same calculation as in (*A*), except that the image was computed according to the method of $O_2$.

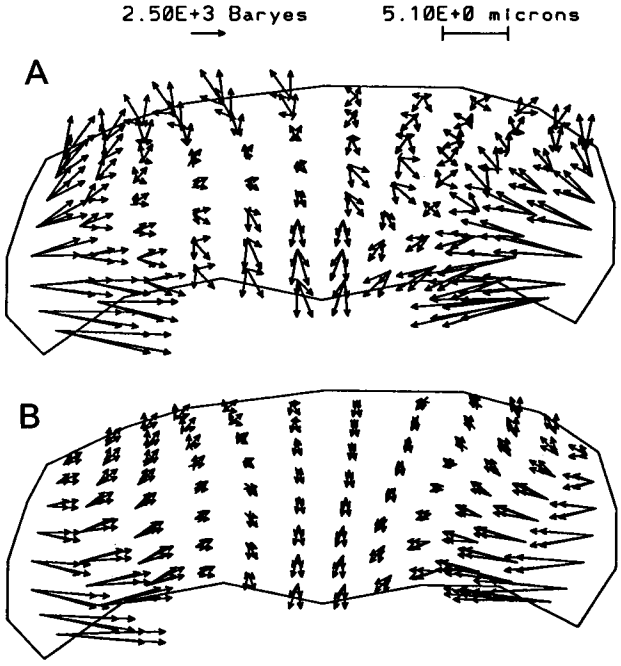


FIGURE 7 Bootstrap analysis of keratocyte traction images. (*A*) Uncertainty of the traction image of Fig. 6 *A*. (*B*) Uncertainty of the traction image of Fig. 6 *B*.

a conservative upper bound on the real dirft error. The fitting procedure of either $O_1$ or $O_2$ is then applied to each of the "bootstrap stimulations" and the results collected to yield a statistical sample of related traction maps. Finally, this sample is used to estimate the standard deviations of the tractions at each mesh node in the usual way. We display the results by plotting a dispersion pattern consisting of the four extreme vectors ($T_1 \pm \delta T_1$, $T_2 \pm \delta T_2$). These form the corners of the 65% confidence "box" bracketing the local traction density field.

Fig. 7 *A* and *B* shows the bootstrap dispersion patterns of the high-resolution traction images of Fig. 6 *A* and *B*, respectively. We conclude that at least the major features of the maximum-likelihood traction images of both observers are well supported and are not substantially affected by the uncertainty of the data. The maximum uncertainty is associated with the small vectors located at the anterior margins.

For rapidly moving cells another source of error in traction images arises because of the finite viscoelastic response time of the silicone rubber films (~1 s, as mentioned above). In essence all particles move less than they would for an instantaneous response time, but the correction is greater for particles in front of the cell than for the particles behind. From dimensional analysis the magnitude of the resulting correction to particle displacement is of the order of the product of the response time and the cell velocity. This number is less than 0.01 $\mu$m in the case of the fish keratocyte and can therefore be safely neglected compared with the other errors discussed previously.

## MISCELLANEOUS REMARKS

It is of interest to check our current estimate of the gross area-averaged traction stress between a keratocyte and its substratum with previous measurements of similar quantities. One such measurement is provided by the microneedle retraction study of Felder and Elson (1990). These authors reported that a stress of $\sim 5 \times 10^2$ dyn/cm$^2$ was exerted by the leading lamella of a fibroblast in the action of retracting a calibrated microneedle adherent to its upper surface. Another approach to measurement of average traction stress is provided by the data of Usami et al. (1992) on the motion of a leukocyte into a capillary tube against counterpressure. Because the contact area between the leucocyte and the capillary wall is ~2 times the cross-sectional area of the capillary in Usami's study, the average tangential stress against the wall must be approximately half of the stall pressure. The result is then an estimated traction stress for the leucocyte of $\sim 8 \times 10^3$ dyn/cm$^2$. Remarkably, both of these estimates of traction stress are in order-of-magnitude agreement with our own estimate ($\sim 2 \times 10^3$ dyn/cm$^2$). One is therefore encouraged to believe that there is some broad consistency among these various determinations of cell-generated traction stress despite big differences in the experimental details.

According to our results, a locomoting keratocyte exerts a characteristic traction force of $\sim(2.2 \times 10^3$ dyn/cm$^2) \times (6.5 \times 10^{-6}$ cm$^2) = 1.4 \times 10^{-2}$ dyn. This value exceeds previous estimates, based on micromanipulation, by a factor of 5 (Lee et al., 1994). Possible reasons for this discrepancy were discussed above (see Studies of Film Rheology, above). For comparison with our total force estimate, recent measurements indicate that the force exerted by single myosin motor is only $10^{-7}$ dyn (see Ishijima et al., 1991). Therefore, it would seem that $\geq 10^5$ myosin motors would be required for the tractions that we observe. Actually this is probably a rather conservative lower bound because the force-generating efficiency of myosin in realistic practice is apt to be very low. In any event, based on studies of amoeba (Clark and Spudich, 1974; Warrick and Spudich, 1987), there would seem to be adequate conventional myosin ($\sim$0.5% of total protein) to generate the required force.

For various purposes, the traction forces involved in cell motility are sometimes classified as propulsive (tending to favor forward motion of the cell), retarding (tending to inhibit this motion), or neutral (normal to the direction of locomotion). Thus in some models actomyosin motors produce propulsive tractions, the peeling of adhesive bonds produce retarding tractions, and there are no neutral tractions (reviewed by Lee et al., 1993). Unfortunately, such anthropomorphic classification of traction stresses are dangerous, particularly when one is attempting mechanistic interpretations of quantitative traction images such as result from our methodology. Thus, it is tempting to conclude from Fig. 5 *B* and *C* that the main or only retarding tractions are at the anterior edge of the lamella and the main or only propulsive tractions are at the posterior edge of the cell. Unfortunately, this sort of conclusion is erroneous. The correct conclusion from our result is that there are local net propulsive and retarding tractions at the respective loci in question. Thus it is perfectly feasible to suppose that rearward actomyosin generated tractions and forward peeling tractions both exist and commingle at all points in the contact region but with the retarding tractions slightly dominant at the front of the cell and the propulsive tractions slightly dominant at the posterior.

In view of such subtleties, it is too early to speculate about the general mechanisms of cell motility based only on the pattern of tractions exhibited by the freely locomoting keratocyte. At a minimum the traction images of different cell types, cells working against different external loads, cells moving at different steady velocities, cells changing directions, and cells moving under conditions of weaker or stronger adhesion should all be quantitatively examined before one reaches conclusions. Moreover this information needs to be carefully integrated with the results of cytology, biochemistry, and genetics and with other biophysical approaches.

Much of the software described in this publication was written when one of the authors (M.D.) was on sabbatical at the Institute for Mechanics and Materials at the University of California, San Diego. Special thanks for hospitality and useful conversations go to the staff of the institute, particularly the director, Prof. R. Skalak.

Work was supported by NIH grant GM 35325 (to K.J.) and NIH grant AI21002 (to M.D.).

## REFERENCES

Bernardo, J. M., and A. F. M. Smith. 1994. Bayesian Theory. John Wiley & Sons, Chichester, UK.

Clark, M., and J. A. Spudich. 1974. Biochemical and structural studies of actomyosin-like proteins from nonmuscel cells: isolation and characterization of myosin from amoeba of *Dictyostelium discoidium*. *J. Mol. Biol.* 86:209–222.

Condeelis, J. 1993. Life at the leading edge: the formation of cell protrusions. *Ann. Rev. Cell Biol.* 9:411–444.

Cramer, L., T. J. Mitchison, and J. A. Theriot. 1993. Actin dependent motile forces and cell motility. *Curr. Opin. Cell Biol.* 6:82–85.

Efron, B., and R. Tibshirani. 1986. Bootstrap methods for standard errors, confidence intervals, and other measures of statistical accuracy. *Statist. Sci.* 1:54–77.

Evans, E. 1993. New physical concepts for cell amoeboid motion. *Biophys. J.* 64:1306–1322.

Felder, S., and E. Elson. 1990. Mechanisms of fibroblast locomotion: analysis of forces and motions at the leading lamellas of fibroblasts. *J. Cell Biol.* 111:2513–2526.

Harris, A. K., P. Wild, and D. Stopak. 1980. A new wrinkle in the study of locomotion. *Science.* 208:177–179.

Harris, A. K. 1984. Tissue culture cells on deformable substrata: biomechanical implications. *J. Biomech. Eng.* 106:19–24.

Ishijima, A., T. Doi, K. Sakurada, and T. Yanagida. 1991. Subpiconewton force fluctuations of actomyosin in vitro. *Nature (London).* 352: 301–306.

Landau, L. D., and E. M. Lifshitz. 1986. Theory of Elasticity, 3rd ed. J. B. Sykes and W. H. Reid, translators. Pergamon Press, Oxford, UK.

Lee, J., A. Ishihara, and K. Jacobson. 1993. How do cells move over surfaces? *Trends Cell Biol.* 3:366–370.

Lee, J., M. Leonard, T. N. Oliver, A. Ishihara, and K. Jacobson. 1994. Traction forces generated by locomoting cells. *J. Cell Biol.* 127: 1957–1964.

Lauffenburger, D. A. 1991. Models for receptor mediated cell phenomina. *Ann. Rev. Biophys. Chem.* 20:387–414.

Oliver, T., M. Dembo, and K. Jacobson. 1995. Traction forces in locomoting cells. *Cell Motil. Cytoskeleton.* 31:225–240.

Sheetz, M. P. 1994. Cell migration by graded attachment to substrates and contraction. *Seminars Cell Biol.* 5:149–155.

Timoshenko, S. 1934. Theory of Elasticity. McGraw-Hill, New York.

Press, W. T., B. P. Flannery, S. A. Teukolsky, and W. T. Vetterling. 1989. Numerical Recipes: The Art of Scientific Computing. Cambridge University Press, Cambridge, UK.

Usami, S., S-L. Wung, B. A. Skierczynski, R. Skalak, and S. Chien. 1992. Locomotion forces generated by a polymorphonuclear leukocyte. *Biophys. J.* 63:1663–1666.

Warrick, H., and J. A. Spudich. 1987. Myosin structure and function in cell motility. *Ann. Rev. Cell Biol.* 3:379–421.